Petroleum Science 23 (2026) 4634–4643

Contents lists available at ScienceDirect

Petroleum Science

journal homepage: www.keaipublishing.com/en/journals/petroleum-science

Original Paper

# Experimental study on the zonal isolation performance of cement sheaths with SBT logging

Xue-Lian Chen [a,b], Fang-Fang Zhao [a,b], Cong-Hui Zhang [c], Xin-Yang Guo [a], Xiao-Ming Tang [a,b,*]

[a] State Key Laboratory of Deep Oil and Gas, China University of Petroleum (East China), Qingdao, 266580, Shandong, China
[b] School of Geosciences, China University of Petroleum (East China), Qingdao, 266580, Shandong, China
[c] China Oilfield Services Limited, Beijing, 101149, China

ARTICLE INFO

*Article history:*
Received 10 December 2025
Received in revised form
15 January 2026
Accepted 24 March 2026
Available online 30 March 2026

Edited by Meng-Jiao Zhou

*Keywords:*
Cement sheath
Isolation testing
Interface debonding
SBT logging
Pressure differential

ABSTRACT

The integrity of the cement sheath's zonal isolation in oil and gas wells is a crucial safeguard for safe production and operations in oilfields. However, the zonal isolation integrity of the cement sheath depends on various factors. Currently, there are no established evaluation methods and workflows for quantitatively assessing the interlayer isolation performance of the cement sheath. We developed a full-scale cased-hole testing device for simulating downhole conditions and measuring the isolation performance of cement sheaths. Using this device, we quantitatively monitored the hydraulic sealing pressure differentials of conventional Class G cement versus lightweight cement. Additionally, a Segmented Bond Tool was installed on the inner wall of the casing to monitor the variation trend of the casing-wave amplitude and attenuation during the cement setting and isolation performance testing processes. The experimental results indicate that as the cement gradually sets, its strength increases and the attenuation progressively rises. After the cement strength stabilizes, pressure is applied through the injection port at the bottom of the first interface of the cement sheath. Once the pressure exceeds the hydraulic bonding strength at the interface between the casing and the cement sheath, debonding gradually occurs. The isolation pressure differential of conventional cement is greater than that of lightweight cement. Changes in casing-wave amplitude across various sectors demonstrate that the debonding fracture initiates from the injection port, through the entire circumference of the cement sheath, and then propagates upward along the axial direction. If the cemented sheath has a poorly bonded sector, channeling will initiate from this weakly bonded section and subsequently propagate circumferentially throughout the entire annulus. The experimentally measured hydraulic bonding strength or the isolation pressure differential of the cement sheath can provide reference data for on-site testing or the design of safe production pressure differential schemes.


## 1. Introduction

The zonal isolation integrity of the cement sheath is a critical indicator of cementing quality in oil and gas wells, directly affecting wellbore integrity, reservoir protection, and long-term production safety (Wu et al., 2024; Hao, 2022). With the rapid advancement of unconventional oil and gas development (e.g., shale gas and tight oil) and the increasing exploitation of deep and ultra-deep wells, testing and evaluation methods for cement sheath isolation performance must be continuously improved.

Cement sheath isolation integrity is governed by multiple interacting factors, including interfacial bonding strength, bonding morphology, isolation interval length, and the interzonal pressure differential encountered during testing or production operations (Yan et al., 2024; Wang et al., 2025). These coupled, multi-factor effects highlight the need for a comprehensive quantitative evaluation framework for cement sheath isolation performance, capable of capturing both the initiation and propagation of isolation failure.

At present, commonly used cement isolation evaluation charts in oilfields are largely compiled empirically from field testing or

* Corresponding author.
*E-mail address:* tangxiam@aliyun.com (X.-M. Tang).
Peer review under the responsibility of China University of Petroleum (Beijing).

https://doi.org/10.1016/j.petsci.2026.03.051
1995-8226/

production data, with limited theoretical support and insufficient experimental underpinning (Wei, 2010). Extensive research has been conducted on cement sheath isolation integrity through experimental measurements, numerical simulations, and evaluation-method development (Corina et al., 2019; Ramadan et al., 2019; Bu et al., 2020; Deng et al., 2020, 2023; Wang and Feng, 2024; Congro et al., 2024; Hu et al., 2025). However, effective quantitative methods for the evaluation of cement sheath isolation performance—especially those grounded in full-scale experimental evidence—remain insufficiently developed.

Prior studies have clarified several important mechanisms. Kim et al. (2016) demonstrated that low cement cohesive strength during hydraulic fracturing can trigger shear failure at the cement–casing interface, enabling fractures to propagate rapidly along the interface. Lecampion et al. (2013) conducted experiments and developed a mathematical model for fluid-driven debonding in the annular wellbore space, describing debonding expansion in both circumferential and axial directions. Simulations by Wang and Dahi Taleghani (2014) showed that radial and tangential stresses at the casing–cement interface play important roles in failure propagation, while shear stress significantly affects failure initiation.

Experimental platforms and coupled approaches have further expanded understanding of zonal isolation degradation. Zhou et al. (2019) developed a cement sheath isolation evaluation device and investigated zonal isolation performance under temperature and pressure changes, interface contamination, and aged-cement conditions. Wu et al. (2018) investigated the propagation mechanisms of channeling pathways during cement sheath isolation failure through experimental evaluation of zonal isolation. Du et al. (2021) established a positive linear correlation between cement bond length and zonal isolation integrity, showing that extended bond length substantially improves resistance to fluid channeling. Arjomand et al. (2018) combined experimental and numerical approaches to investigate the integrity of cement and casing under elevated pressure, analyzing the effects of in-situ stress orientation, surrounding-rock stiffness, and casing eccentricity on cement and interface integrity. Feng et al. (2017) employed a pore-pressure-coupled cohesive zone method to simulate the fluid-driven debonding process between casing and the cement sheath. Their results indicated that pre-existing interfacial defects significantly reduce hydraulic isolation pressure and that debonding fractures propagate preferentially along the casing rather than circumferentially along the interface.

To address these limitations, we constructed a full-scale laboratory apparatus capable of simulating downhole high-temperature and high-pressure conditions, in order to measure the zonal isolation performance of the cement sheath. The experimental setup measured the hydraulic bonding strength at cement–casing interfaces. Importantly, a Segmented Bond Tool (SBT) was employed to monitor the propagation of debonding fractures at the first interface of the cement sheath. The trend of casing-wave amplitude variation across sectors revealed that interface debonding in full-scale casing wells initiates around the circumference of the casing–cement interface and then extends axially.

## 2. Experimental measurement system

The schematic diagram of the cement sheath isolation testing device is shown in Fig. 1. The experimental setup used actual oil well casing and cement slurry. It incorporated a casing with an outer diameter of 177.8 mm and a wall thickness of 12.56 mm, a borehole diameter of 215.9 mm, a cement sheath with a placement length of approximately 1070 mm, and a sandstone formation with

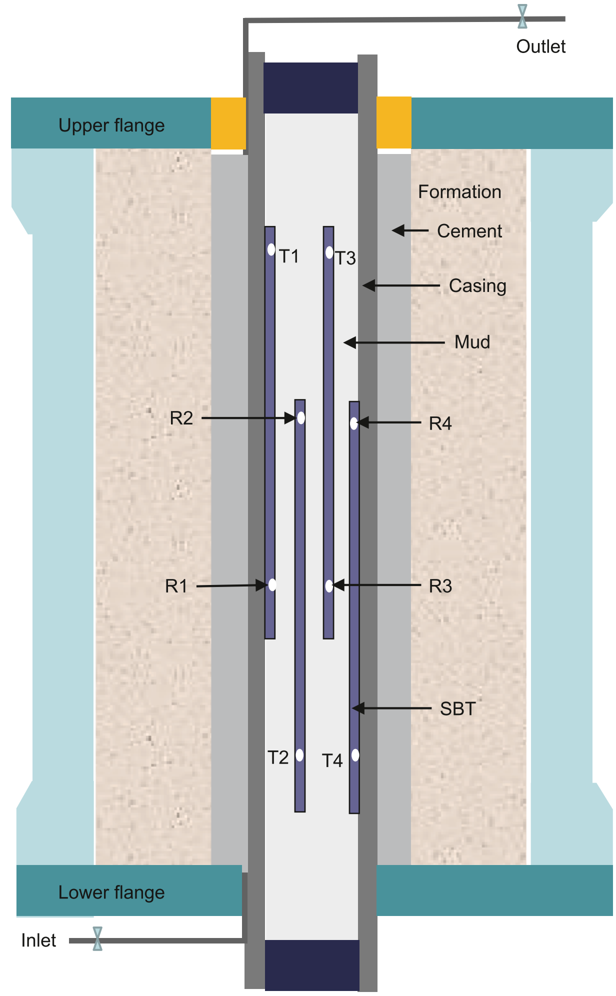


**Fig. 1.** Schematic diagram of the cement isolation performance testing device. The SBT is used to monitor the cement bonding condition during isolation performance testing process.

a radial thickness of 200 mm. The entire cased-hole model was housed within a temperature-pressure-controlled vessel during testing. Following cement placement, separate pressure systems were used to apply 20 MPa to the casing interior and cement sheath, and 40 MPa confining pressure to the formation. The temperature of the entire cased-hole model is maintained at around 60 °C through a heat transfer oil circulation system. Zonal isolation performance testing of the cement sheath was initiated after 48 or 72 h of curing. Gas-driven or water-driven pressure (also known as a gas or water channeling experiment) was applied at the bottom inlet to gradually increase the differential pressure across the cement sheath, while monitoring the pressure variation at the upper outlet. A sharp pressure rise at the upper outlet usually results from effective fluid channeling and pressure communication, which serves as an indication of zonal isolation failure. The corresponding pressure increment at the inlet under these conditions is defined as the zonal isolation pressure differential across the cement sheath. The Segmented Bond Tool (SBT) is fixed upon the inner wall of the casing. Throughout the experiment process, the casing-wave amplitudes received by the SBT receivers and the attenuations recorded by the compensated acoustic system can be continuously used to monitor the bonding condition of the cement sheath. The casing-wave amplitudes recorded by the SBT logging tool across different sectors effectively and clearly demonstrated the gradual debonding or bonding failure at the casing–cement interface as the inlet pressure increases (Liu et al., 2024).

The SBT consists of six pads, which are placed against the inner casing surface to measure the casing-wave attenuation. Each pad is equipped with one transmitter and one receiver. Each transmitter is equipped with two emission units. Through phase control, the radiated acoustic waves are steered toward the receivers located on the adjacent pads. The transmitter's working frequency ranges from 80 kHz to 100 kHz (Wei, 2010). The six pads are evenly distributed in the circumferential direction, and adjacent pads are staggered in the axial direction, as shown in Fig. 1. The axial positions of the alternating pads are aligned so that every four adjacent pads form a dual-transmitter and dual-receiver attenuation rate measurement scheme. The entire circumference is evenly divided into six sectors, and the attenuation rate in each of the six sectors can be measured separately. For example, T1 transmits, near R2 and far R3 receive; T4 transmits, near R3 and far R2 receive. The combination T1–R2–R3–T4 forms a compensated attenuation measurement scheme. The formula for calculating the attenuation rate is shown in Eq. (1), and its value represents the attenuation rate measured in the sector between the second pad (R2) and the third pad (R3). In addition to the attenuation rate, the amplitude of the casing wave received by each receiver can reflect the bonding condition along the cylindrical propagation path from the transmitter to the receiver. For instance, during the isolation test, the amplitude $A_{12}$ of the casing wave received by R2 when T1 transmits can reflect the cement bonding condition along the path from T1 to R2. The amplitude $A_{43}$ received by R3 when T4 transmits can reflect the bonding changes along the path from T4 to R3. The two sectors corresponding to the T1–R2 and T4–R3 propagation paths are located at different axial and circumferential positions along the cased-hole model. By monitoring the amplitude of the casing waves at the 12 near receivers, the progressive development of interfacial debonding fracture from the lower to the upper part of the cement sheath can be characterized in greater detail during isolation performance testing process.

The attenuation rate is defined by the following equation:

$$Att = 10 / D \times \log_{10}[(A_{12} \times A_{43}) / (A_{13} \times A_{42})], \quad (1)$$

where $Att$ represents the attenuation rate, $D$ is the cylindrical propagation distance of the casing wave between the near and far receivers, and $A_{ij}$ is the casing wave amplitude emitted by the $i$-th transmitter and received by the $j$-th receiver.

## 3. Impact of microannulus between casing and cement sheath on SBT logging response

During the gas or water-driven isolation testing process, debonding between the casing and the cement sheath can easily form a microannulus. SBT logging, which is sensitive to microannuli, can effectively capture this effect. The SBT tool employs a compact transmitter whose vibrations are localized to a small area of the casing's inner wall and operates at high frequencies (80 kHz to 100 kHz). Under these conditions, the casing wave excited in the casing can be treated as a zero-order symmetric Lamb wave ($S_0$ mode) in a plate. The propagation of the $S_0$ Lamb wave within the casing is predominantly governed by axial displacement in the 80–100 kHz frequency band (Wang et al., 2020). Energy leakage from the casing into the surrounding media primarily depends on shear coupling at the interfaces (Chen et al., 2020). During isolation test, the formation of a flow pathway allows fluid (water or gas) to infiltrate the casing–cement interface, breaking the interfacial shear coupling. This bonding failure at the interface results in a pronounced increase in casing-wave amplitude accompanied by reduced attenuation. Fig. 2 presents the theoretical dispersion and attenuation characteristics of zero-order symmetric Lamb waves. The phase velocity of the $S_0$ modal wave is not sensitive to the bonding condition or the presence of microannuli, but the attenuation values change significantly. When cement with a density of 1.9 g/cm$^3$ is bonded to the casing, the attenuation of the zero-order symmetric Lamb wave approaches 10 dB/ft. The acoustic and mechanical properties of cements are shown in Table 1. As the cement density reduces, the attenuation decreases. In the presence of a 0.01 mm-thick wet microannulus between the casing and the cement sheath (e.g. water-driven isolation test), the attenuation significantly decreases, approaching the attenuation value of a free casing. If the microannulus is gas-filled, the attenuation falls below the attenuation value of a free casing. Therefore, if channeling or pressure transmission occurs between the casing and the cement sheath during the isolation testing experiment, the SBT logging will show a clear decrease in attenuation and an increase in casing-wave amplitude. This provides an effective real-time monitoring method for indicating debonding between the casing and the cement sheath during the isolation testing process.

## 4. Experimental results of cement sheath isolation performance test

### 4.1. Isolation performance test of conventional cement sheath with a density of 1.9 g/cm$^3$

After pouring the Class G cement with a density of 1.9 g/cm$^3$, the flange on the vessel was installed, and pipelines were connected to ensure sealing. Pressure tests were then separately conducted on the casing interior, the cement sheath, and the annulus between the formation and the vessel. Once effective sealing was confirmed, the measurement device was heated and pressurized. The pressure inside the casing and on cement sheath were both set to 20 MPa, while a horizontal stress of 40 MPa was applied to the outer wall of the formation, with the temperature controlled at around 60 °C. After the temperature and pressure stabilization, the SBT began recording logging data in time acquisition mode. Fig. 3 shows the attenuation values recorded in the six circumferential sectors during the cement setting process. The attenuation remained almost constant at approximately 4 dB/ft in the first 6 h after cement pouring. Between 7 h and 15 h, the attenuation increased sharply, indicating a rapid increase in cement strength during this period. From 15 h to 40 h, the attenuation increased slowly and gradually stabilized.

#### 4.1.1. Analysis of gas-driven isolation performance test results

Apply gas pressure through the inlet at the bottom of the cement sheath after the cement has set and gained sufficient strength. This gas channeling test is used to evaluate the hydraulic bond strength at the cement–casing interface. To visualize the gas-driven channeling process along the cement interface, the combined variations in casing-wave amplitude and attenuation—recorded by SBT's transmitter-receiver arrays positioned at different circumferential and axial locations—were used to map the spatial evolution of cement bonding condition, as shown in Fig. 4. The interface between the casing and the cement sheath is partitioned into 18 zones. The casing-wave amplitude variations in specific paths, including T2–R1, T2–R3, T4–R3, T4–R5, T6–R5, and T6–R1, serve to diagnose bonding integrity and detect the formation of debonding gaps in Sectors 13 through 18 (the area marked with the blue numbers in Fig. 4). In contrast, the six attenuation rates recorded by the SBT tool can reflect the bonding condition of

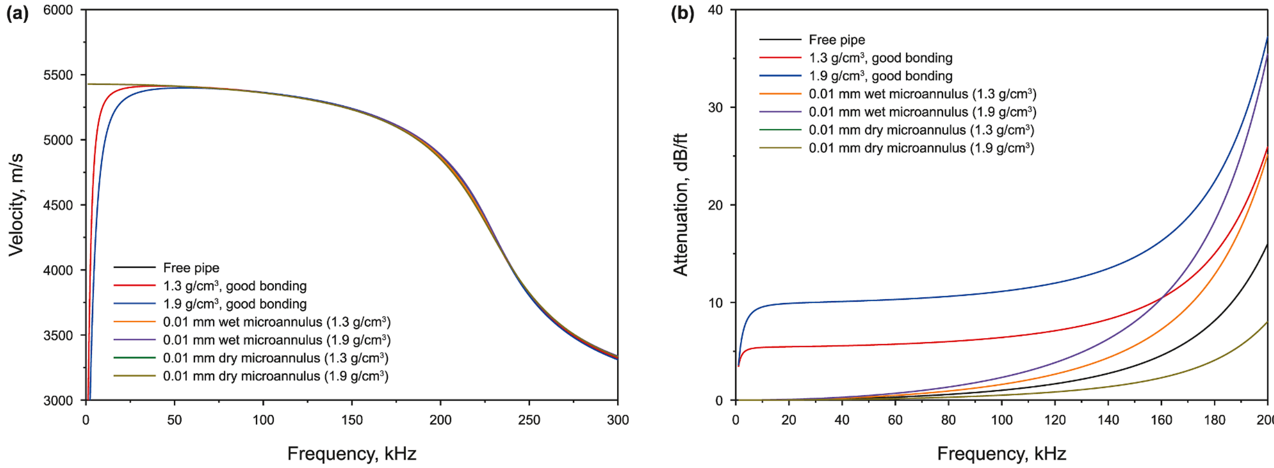


**Fig. 2.** Dispersion **(a)** and attenuation **(b)** curves of the $S_0$ modal waves.

**Table 1**
The acoustic and mechanical properties of cements.

| Property | Lightweight cement | Conventional cement |
|---|---|---|
| Density, kg/m$^3$ | 1500 | 1900 |
| P-wave velocity, m/s | 2755 | 3053 |
| S-wave velocity, m/s | 1473 | 1739 |
| Compressive strength, MPa | 12.0 | 23.1 |

the intermediate Sectors 7 to 12. The interface bonding condition in the upper sectors (Sectors 1 to 6) can be characterized by the variations in casing-wave amplitude from the following transmitter-receiver combinations: T1–R2/R6, T3–R2/R4, and T5–R4/R6.

Fig. 5 illustrates the variation in casing-wave amplitude with testing time during the gas-driven isolation process. At 200 s, the inlet pressure at the bottom end of the cement sheath (blue curve in the rightmost track) was gradually increased using an air pump in 0.5 MPa increments. During the initial pressurization stage, the outlet pressure at the top end (red curve in the rightmost track) remained relatively stable. As the inlet pressure continued to rise, the outlet pressure also increased slightly between 300 s and 628 s. This change was not caused by interface debonding, as the pressure difference between the two ends of the cement sheath continued to show an increasing trend, and the casing-wave amplitudes measured in each sector remained unchanged. This indicates that the inlet pressure had not yet reached the breakthrough pressure of the cement sheath's first interface, and the interface remained well-bonded. However, due to the permeability of the cement or disturbances in the pressure system, the outlet pressure may increase slightly when the inlet pressure rises significantly. Therefore, to accurately determine the effective hydraulic bonding strength at the cement–casing interface, the inlet pressure can be increased after the outlet pressure has stabilized following each increment. At 628 s, the inlet pressure increased to 27.59 MPa. At this point, the outlet pressure began to rise more rapidly, exceeding the rate of increase of the inlet pressure, which resulted in a gradual reduction of the pressure difference between the upper and lower ends of the cement sheath. According to the casing-wave amplitudes measured by the SBT, the amplitudes in Sectors 13 to 18, which are closest to the bottom inlet of the cement sheath, showed a significant increase, as indicated by the black horizontal solid line in Fig. 5. This suggests that the lower section of the first interface of the cement sheath had been breached circumferentially. As the inlet pressure continued to rise, around 638 s, the casing wave amplitudes in Sectors 1 to 6 also began to gradually increase, as marked by the

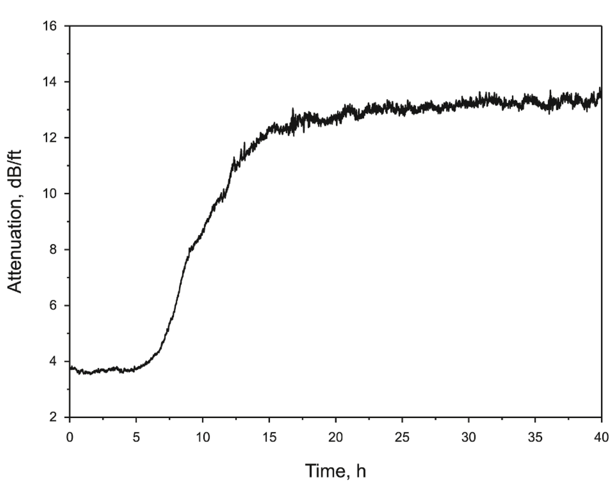


**Fig. 3.** Attenuation measured by SBT during cement setting.

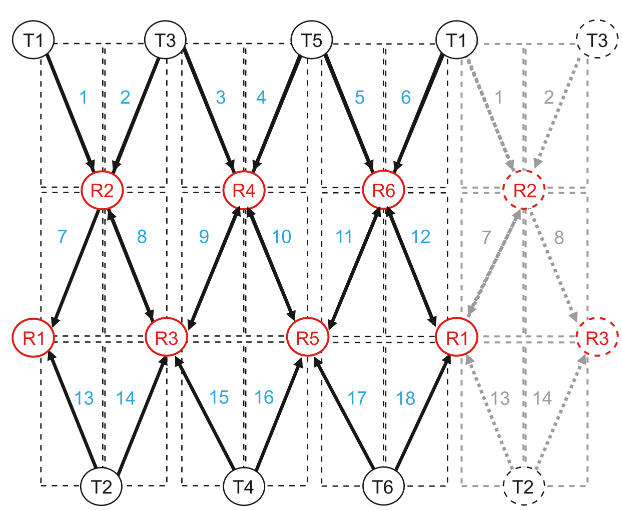


**Fig. 4.** A Sector-based bonding map scheme for measuring the cement sheath's first interface.

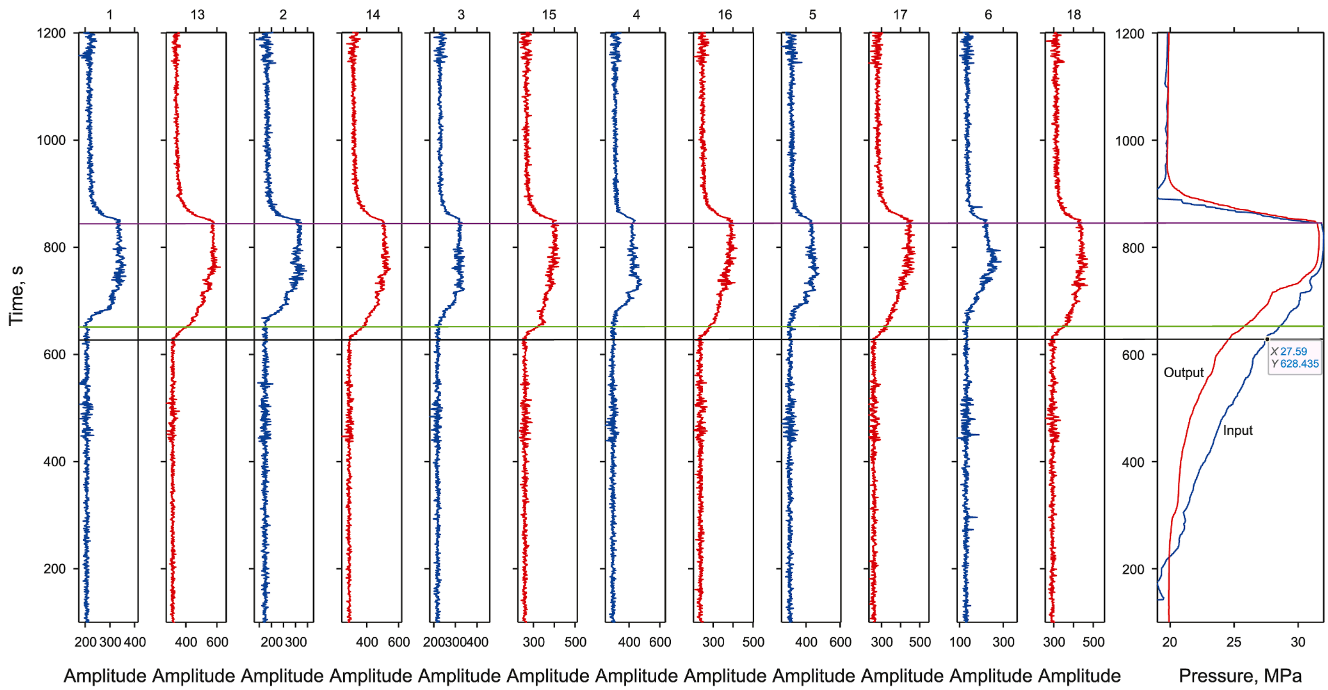


**Fig. 5.** The variation trend of the casing-wave amplitude during the gas channeling process.

green solid line in Fig. 5. This indicates that the debonding fracture at the first interface of the cement sheath had extended to the upper half of the cased-hole model. When the inlet and outlet pressures converged, it indicated that the entire cement sheath had become fully channeled. At the time marked by the purple solid line in Fig. 5, the inlet pressure was released, and the outlet pressure also gradually decreased. Meanwhile, the casing-wave amplitudes monitored across the entire cement sheath showed a gradual reduction, indicating that the microannulus at the first interface caused by gas channeling was slowly closing. The combination of casing-wave amplitude variations in each sector and the changes in outlet pressure clearly demonstrates the gradual process of gas channeling verification in the cement sheath and the progressive failure of bonding at the casing–cement sheath interface.

The isolation differential pressure test result of the cement sheath may be influenced by the pressurization rate. As such, for the cased-hole model used in Fig. 5, the pressure loading rate was reduced, and the holding time between increments was increased. The corresponding results are shown in Fig. 6. Compared with the results in Fig. 5, the time difference between the onset of casing-wave amplitude increase in the upper and lower sectors became significantly larger. Specifically, the time required for interface debonding fracture to propagate from Sectors 13–18 to Sectors 1–6 increased from the original 10 s to 150 s. When the casing-wave amplitude in the upper sectors of the model had been increasing for approximately 70 s (as shown by the green solid line in Fig. 6), and the inlet pressure reached 31.63 MPa, the outlet pressure exhibited a significant increase. Subsequently, the pressure difference between the inlet and outlet decreased sharply until they converged, indicating the failure of the cement sheath isolation. The slow-pressurization test exhibited a higher isolation pressure differential (or hydraulic bonding strength) relative to the test in Fig. 5. With the subsequent gradual release of the inlet pressure, the casing-wave amplitudes in all sectors progressively decreased.

The interface bonding condition of Sectors 7 to 12 can be evaluated by monitoring variations in attenuation values recorded by the SBT. Fig. 7 presents the correlation between the attenuation measured by the SBT and the pressure variations at the top and bottom of the cement sheath, corresponding to the data in Fig. 6. The black solid lines in Fig. 7 represent six attenuation curves of individual sectors. It can be observed that the attenuation values across all sectors in this cased-hole model follow a consistent trend, indicating that cement debonding is present around the entire circumference. At the moment indicated by the dashed arrow 1 in Fig. 7, the attenuation values decreased significantly across the entire circumference, indicating the formation of a microannulus at the cement–casing interface in Sectors 7 to 12. A slight drop in inlet pressure coincides with a trend of increasing attenuation across all sectors, demonstrating the high sensitivity of the interfacial bonding to pressure perturbations. By arrow 3, the resumption of inlet pressure and a sharp rise in outlet pressure again led to a marked decrease in circumferential attenuation. By the time indicated by arrow 4, the pressures at the top and bottom of the cement sheath had converged, indicating that full channeling had occurred along the entire length of the cement sheath. The attenuation reached its minimum value, while the microannulus thickness resulting from debonding at the casing–cement interface reached its maximum during the entire experiment. As the inlet pressure gradually reduced, the attenuation exhibited a corresponding increase. By arrow 5, following pressure release, the attenuation significantly increases, indicating a substantial reduction in the thickness of the microannulus. This recovery demonstrates the high strength of the cement, as the bonding failure process caused no evident plastic deformation, allowing the attenuation values to progressively return to their pre-test baseline. Fig. 8 shows the photograph of the inner wall of the cement sheath after the isolation test. The inner wall of the cement sheath appears smooth.

#### 4.1.2. Analysis of water-driven isolation performance test results

The hydraulic bonding strength of the cement sheath in the experimental setup was also measured by pressurizing the inlet end with water. Fig. 9 shows the variation in casing-wave

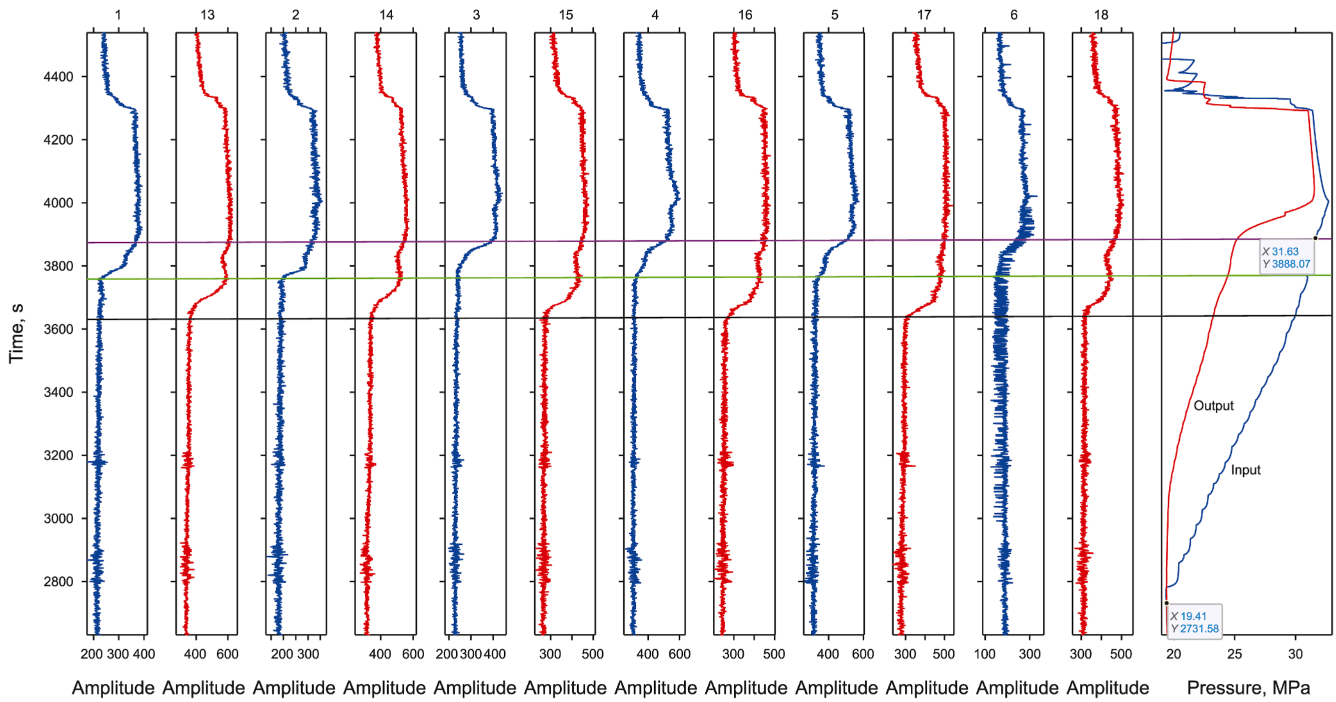


**Fig. 6.** Casing wave amplitude variation during the slow-pressurization gas channeling process.

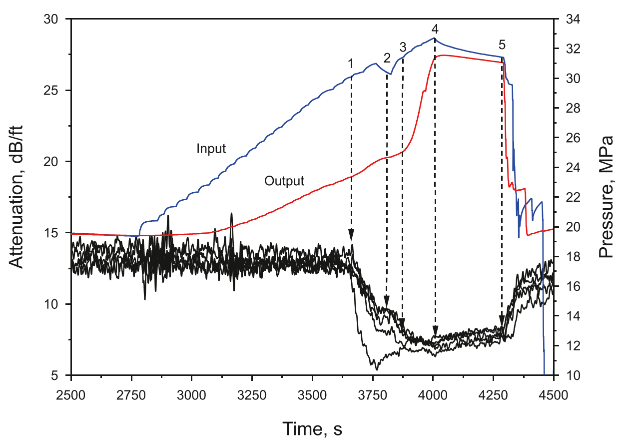


**Fig. 7.** The variation trend of casing-wave attenuations during the gas channeling process.

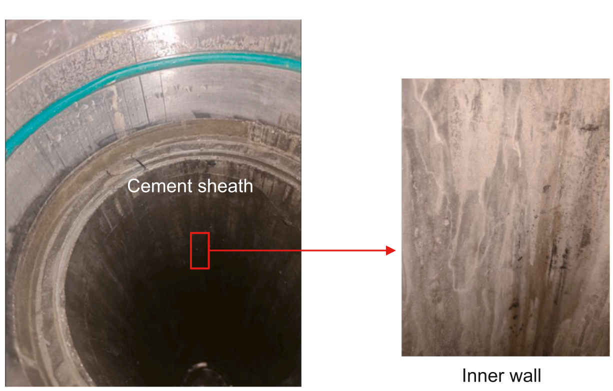


**Fig. 8.** A photo of the inner wall of the cement sheath after the isolation test.

amplitude in the upper and lower sectors during the test. As the inlet pressure was increased slowly in fixed increments, a significant rise in casing-wave amplitude was observed in Sectors 13–18 at 5490 s, as marked by the black solid line in Fig. 9. At this point, the amplitude in the upper sectors remained unchanged, suggesting that the interface at the lower end of the cement sheath had been breached while the bonding in the upper zones remained intact. Based on the trend of the casing-wave amplitude increase, the propagation rate of the interfacial debonding fracture during the water channeling test was noticeably slower than during gas channeling, with a more gradual amplitude growth. Around 5600 s, the casing-wave amplitude in the upper sectors began to increase gradually, but the cement sheath had not yet been fully breached. At the time marked by the purple solid line, the outlet pressure began to rise sharply, indicating that the cement sheath had separated from the casing due to complete debonding at the interface. At this point, the inlet pressure had increased by 11.35 MPa, indicating that the isolation pressure differential across the entire cement sheath, which represents its hydraulic bonding strength, was 11.35 MPa.

During the water channeling process, the attenuation values measured by the SBT tool are shown in Fig. 10. At the time indicated by arrow 1, the attenuation begins to gradually decrease. At arrow 2, the outlet pressure increases sharply. However, as can be seen at the time marked by arrow 3, when the inlet pressure stabilized and no longer continued to rise, the attenuation remained essentially constant despite the increase in outlet pressure. This indicates that the debonding state at the interface did not continue to propagate. As the inlet pressure continued to rise, at the moment marked by arrow 4, the inlet and outlet pressures tended to equalize, while interfacial bonding failure occurred across the entire interface. The attenuation reached its minimum value. After the pressures of the inlet and outlet were released, the attenuation increased significantly again.

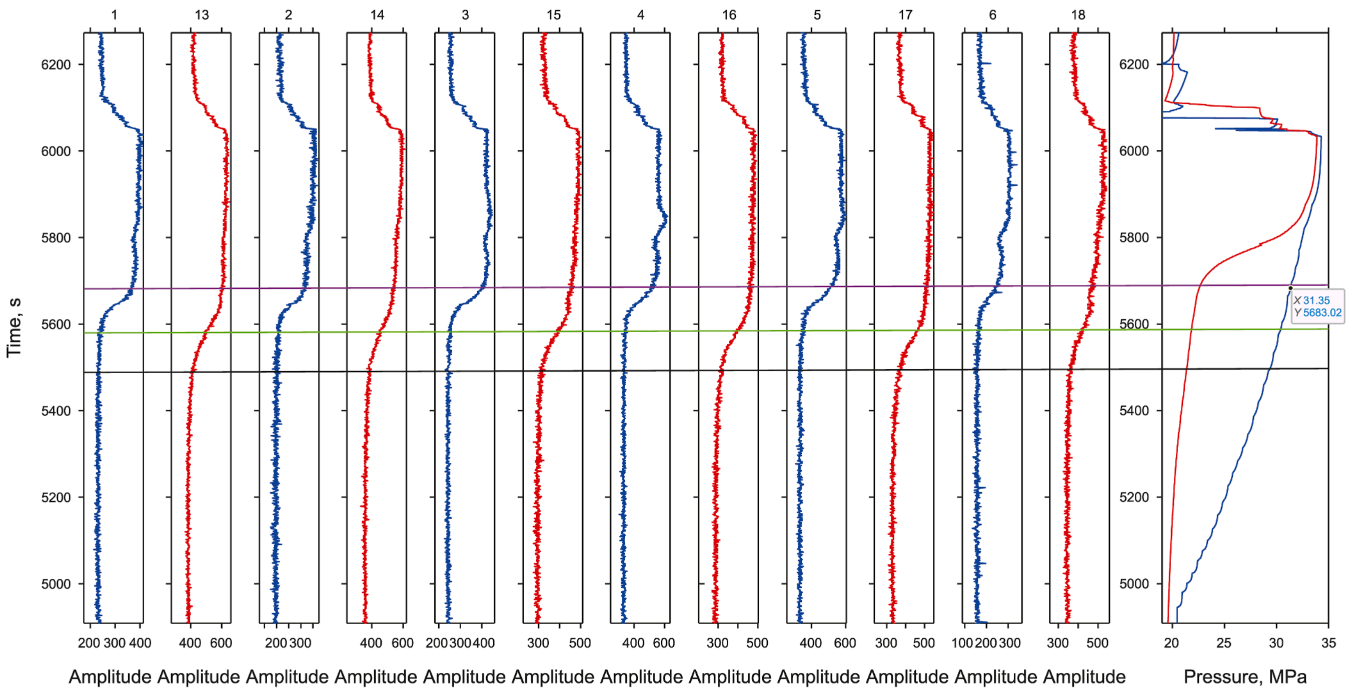


**Fig. 9.** The variation trend of casing-wave amplitude during the water channeling process.

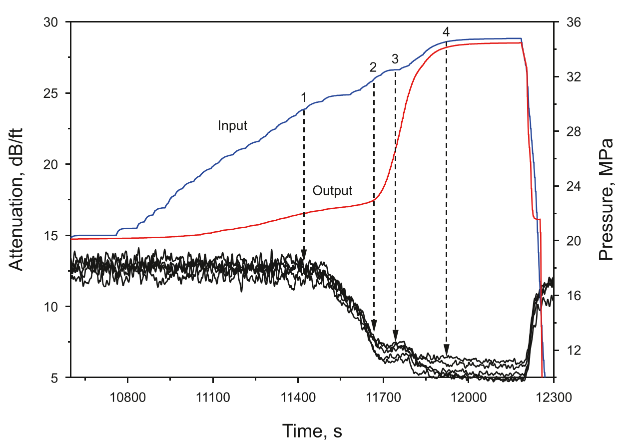


**Fig. 10.** The variation trend of casing-wave attenuations during the water channeling process.

### 4.2. Isolation performance test of lightweight cement sheath with a density of 1.5 g/cm$^3$

The lightweight cement with a density of 1.5 g/cm$^3$ exhibited lower compressive strength than the 1.9 g/cm$^3$ cement. Fig. 11(a) presents the variation of pressure at both ends of the cement sheath and the casing-wave amplitudes recorded by SBT receivers during the gas channeling test. At the moment indicated by arrow 1, as the pressure at the inlet end increases, the rate of pressure increase at the outlet end accelerates. However, there is no significant upward trend in the casing-wave amplitude across all sectors, indicating that the cement sheath interface has not yet been breached at this point, and only the permeability of the cement or the interface has increased. As the inlet pressure continues to rise, at the moment indicated by arrow 2, the casing-wave amplitudes recorded in the lower sectors of the cement sheath increase significantly, indicating that the interface between the casing and the cement sheath near the inlet end has been breached. At this point, the inlet pressure has increased by approximately 7 MPa. From the locally magnified image (from 8200 s to 8550 s) provided in Fig. 11(b), it can be observed that at the moment indicated by arrow 2 in Fig. 11(a), the interface debonding in Sector 18 occurred later than in the other five sectors. At 8300 s, the interface debonding expanded to the upper part of the cement sheath. As the casing-wave amplitudes represented by the black dashed lines in Fig. 11(b) gradually increased, Sector 1 was the first to experience debonding. After approximately 50 s, the casing-wave amplitudes received by the other sectors also began to gradually increase, indicating that the debonding interface progressively extended circumferentially, causing the outlet pressure to approach the inlet pressure more rapidly. During the period between arrow 2 and arrow 3 in Fig. 11(a), the pressure difference between the inlet and outlet gradually decreased, and the casing-wave amplitudes in all sectors gradually increased, suggesting that the gap caused by the bonding failure between the casing and cement sheath gradually widened. After arrow 3, as the loading pressure was released, the casing-wave amplitudes decreased sharply.

During the gas channeling pressurization test, Fig. 12 illustrates the dynamic propagation of the interface debonding across sectors at different time points. The color gradient visually represents the bonding condition of the cement sheath: darker blue indicates better bonding integrity, while darker red reflects more severe debonding. Corresponding to the time marked by arrow 2 in Fig. 11(a), the four snapshots at $t = 8300$ s, $t = 8350$ s, $t = 8375$ s, and $t = 8400$ s in Fig. 12 clearly demonstrate that cement debonding initially propagates predominantly in the circumferential direction. With continued increase in inlet gas-driven pressure (prolonged pressurization time), once the bond failure at the cemented interface in the lower sectors was mostly compromised, debonding began to extend axially along the casing by $t = 8450$ s, while both the extent and severity of circumferential debonding further increased. By approximately $t = 9000$ s, when the inlet and outlet pressures had nearly equalized, the interfacial

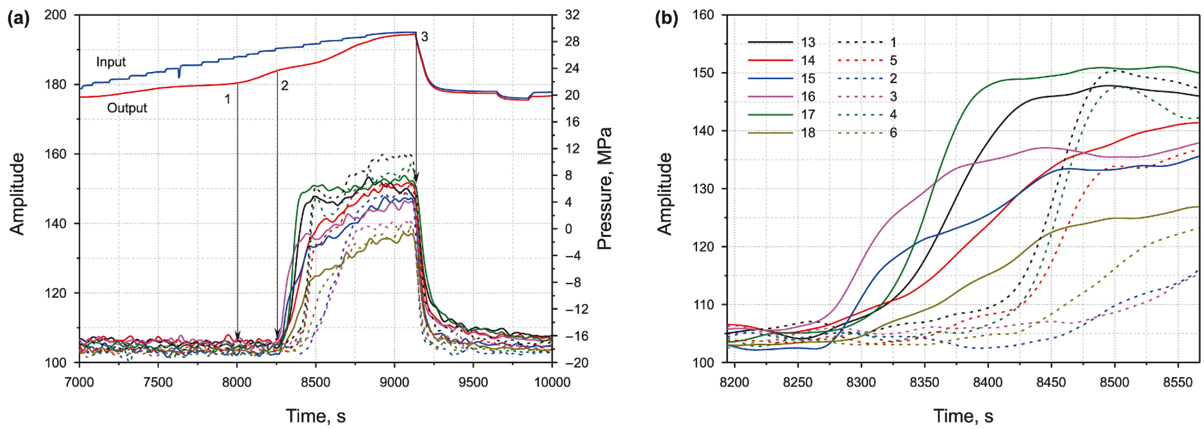


**Fig. 11.** Variation trends of cement sheath upper and lower end pressures and casing-wave amplitudes in each sector during gas channeling test, showing **(a)** the entire gas channeling process and **(b)** the interfacial debonding stage in detail.

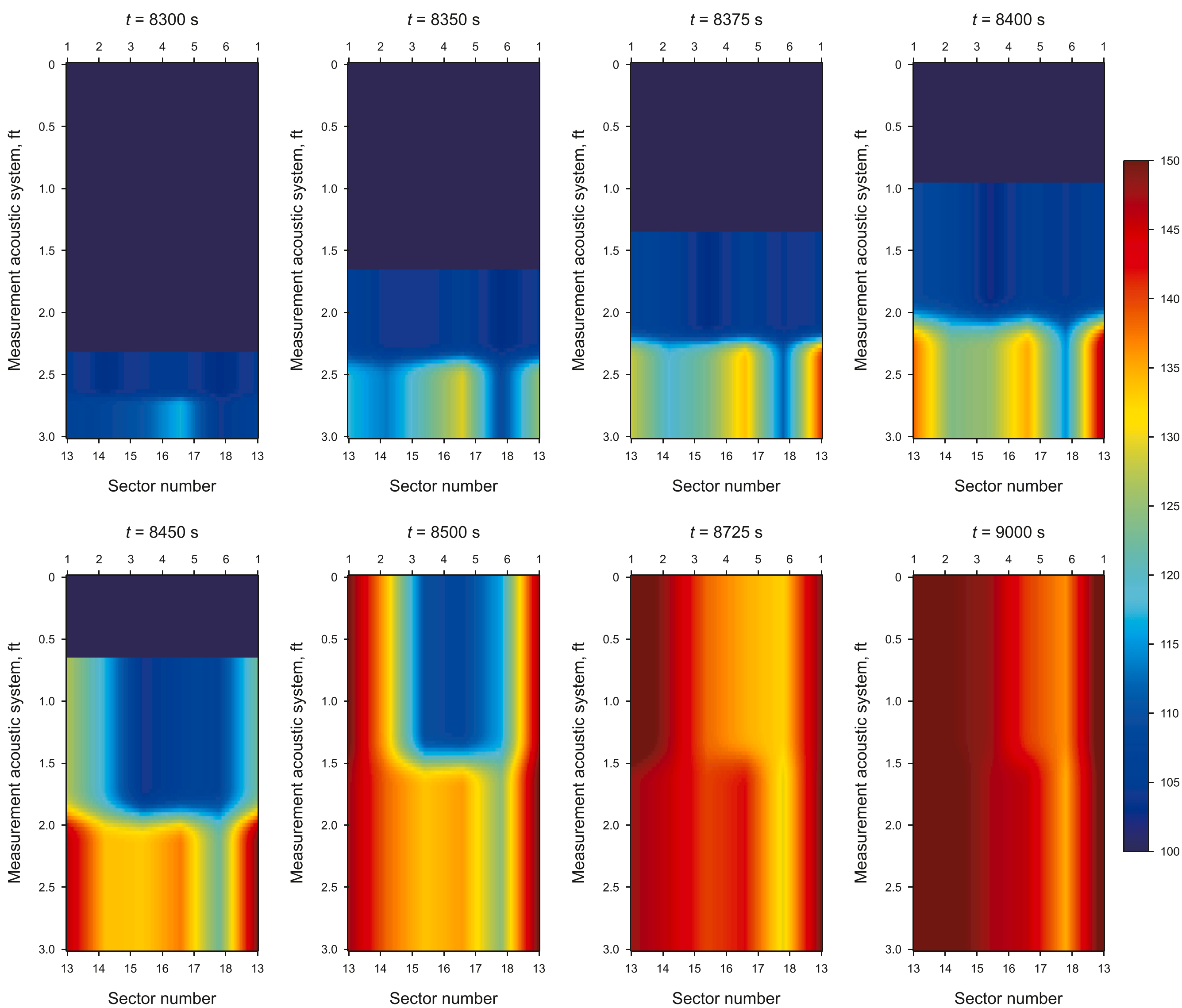


**Fig. 12.** Dynamic evolution of interface debonding at different timestamps during the gas channeling test.

debonding reached its maximum extent, with both upper and lower sectors approaching a completely debonded state. However, analysis of the amplitude dynamic variation across all sectors reveals that Sector 18 experienced delayed and weak debonding compared to the other five sectors, attributable to circumferential heterogeneity in cement bonding quality and/or variations in casing outer wall roughness.

Fig. 13 shows the variation trends of casing-wave amplitudes across all sectors during water channeling. At the position indicated by arrow 1, the casing-wave amplitudes in all sectors had reached their maximum values, while the outlet pressure began to increase at a significantly accelerated rate. This indicates that the first interface of the cement sheath has essentially been breached. The inlet pressure at this point is 27.3 MPa, representing a hydraulic bond strength of approximately 7.3 MPa for the cement sheath, which is lower than the value measured for cement with a density of 1.9 g/cm$^3$. At the time indicated by arrow 2, as both the inlet and outlet pressures were gradually bled off, the casing-wave amplitudes began to decrease, indicating a progressive recovery of bonding at the cement–casing interface.

## 5. Discussion

The experimental results show that, under the same cement density and comparable bonding conditions, water-channeling pressurization leads to a slower progression of interfacial debonding than gas-channeling conditions, and requires a larger pressure increment—i.e., a higher sealing (isolation) pressure differential—to achieve a fully throughgoing leakage path along the entire cement sheath. Mechanistically, for the same microannulus geometry, water has a higher viscosity, is effectively incompressible, and is typically the wetting phase; therefore, pressure within the flow path is more readily dissipated by viscous losses along the path and by wetting/capillary effects. As a result, it is more difficult to develop sufficient localized crack-driving force at the debonding front, such that debonding advances more stably but more slowly, and breakthrough requires overcoming a higher capillary entry pressure and a larger pressure gradient. In contrast, gas has a lower viscosity and is compressible, which more readily promotes tip pressure focusing and interfacial aperture amplification, triggering faster propagation and thus requiring a lower pressure differential.

The differences in sealing pressure differential among cements of different densities indicate that the conventional density cement sheath exhibits a higher isolation load-carrying capacity

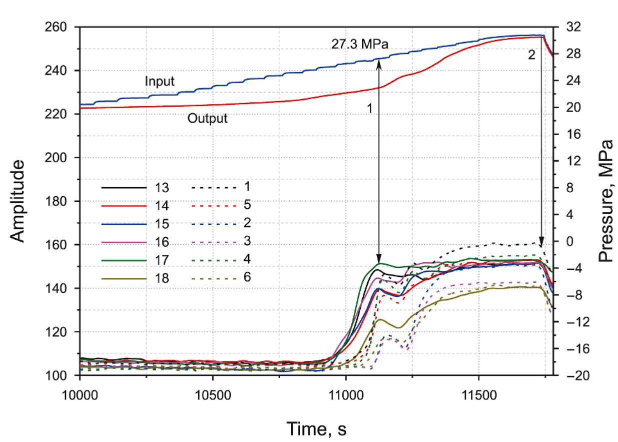


**Fig. 13.** Variation trends of cement sheath upper and lower end pressures and casing-wave amplitudes in each sector during water channeling test.

than the lightweight cement. This difference can be mainly attributed to the higher mechanical integrity (strength and fracture toughness) and lower susceptibility to defects of conventional cement, which increases the pressure threshold required for interfacial debonding, microannulus growth, and leakage-path connectivity. By comparison, due to its strength reduction resulting from density reduction (e.g., hollow microspheres and/or foaming), lightweight cement promotes earlier initiation and propagation of microannuli, thereby allowing continuous leakage pathways to form under lower pressure differentials.

In addition, sectoral poor or circumferentially non-uniform bonding may reduce the sealing pressure by promoting localized leakage-path initiation and earlier breakthrough, and may also lead to earlier changes in diagnostic responses (e.g., attenuation or casing-wave amplitude). Quantifying these effects requires controlled, repeatable sectoral defect geometries and will be addressed in future work.

## 6. Conclusion

The performance of cement sheath zonal isolation was evaluated under controlled experimental conditions. By deploying a segmented bond logging acoustic system inside the casing, the dynamic debonding process of the cement sheath's first interface was monitored during both gas and water channeling. The main conclusions of this study are as follows.

(1) Based on the attenuation from the six sectors of the SBT during cement setting, the actual bonding condition at the casing–cement sheath interface before isolation testing can be determined. When the attenuation values across all six sectors are relatively uniform and reach levels corresponding to their compressive strength, it indicates good bonding integrity around the entire circumference.
(2) During gas or water channeling, the progression of interfacial debonding in both circumferential and axial directions can be delineated by analyzing variations in either casing-wave attenuations or amplitudes across individual sectors. Results of zonal isolation tests conducted with two cement densities show that during water or gas channeling, if circumferential bonding is uniform, interfacial debonding initiates circumferentially until the entire or the majority of sectors are affected, thereafter the debonding extends along the axial direction. In axial debonding, breakthrough usually occurs from the weakest bonding sector.
(3) The combined analysis of casing-wave amplitudes recorded at various axial positions and the dynamic evolution of interfacial debonding at different timestamps demonstrates that the debonding process of water channeling is significantly slower than that of gas channeling. Furthermore, the pressure increment required to achieve complete channeling throughout the cement sheath is notably higher in water channeling compared to gas channeling.
(4) The isolation pressure differential of conventional cement sheath is higher than that of lightweight cement.

## CRediT authorship contribution statement

**Xue-Lian Chen:** Writing – review & editing, Writing – original draft, Visualization, Methodology, Formal analysis, Data curation, Conceptualization. **Fang-Fang Zhao:** Writing – review & editing, Writing – original draft, Visualization. **Cong-Hui Zhang:** Supervision, Resources, Project administration, Methodology. **Xin-Yang Guo:** Validation, Methodology, Investigation. **Xiao-Ming Tang:**

Writing – review & editing, Supervision, Resources, Project administration, Methodology.

## Declaration of competing interest

The authors declare that they have no known competing financial interests or personal relationships that could have appeared to influence the work reported in this paper.

## Acknowledgment

This study was supported by Oil & Gas Major Project (Grant No. 2025ZD1401106) and the National Natural Science Foundation of China (Grant Nos. 42374156 and 41774141).

## References

Arjomand, E., Bennett, T., Nguyen, G.D., 2018. Evaluation of cement sheath integrity subject to enhanced pressure. J. Pet. Sci. Eng. 170, 1–13. https://doi.org/10.1016/j.petrol.2018.06.013.

Bu, Y.H., Ma, R., Guo, S.L., et al., 2020. A theoretical evaluation method for mechanical sealing integrity of cementing sheath. Appl. Math. Model. 84, 439–458. https://doi.org/10.1016/j.apm.2020.03.001.

Chen, X.L., Tang, X.M., Li, S.Q., et al., 2020. Study on the propagation characteristics of the casing waves in cased wells by viscoelastic slip theory. Chin. J. Geophys. 63 (9), 3562–3571. https://doi.org/10.6038/cjg2020N0050 (in Chinese).

Congro, M., Skadsem, H.J., Beltrán-Jiménez, K., et al., 2024. Experimental and numerical study on the pushout shear strength of conventional and expanding cement–casing sections for well integrity. Geoenergy Sci. Eng. 234, 212638. https://doi.org/10.1016/j.geoen.2024.212638.

Corina, A.N., Opedal, N.V., Vralstad, T., et al.. A laboratory study of the effect of casing pipe roughness on cement plug integrity. https://doi.org/10.2118/194158-MS.

Deng, K.H., Yuan, Y., Hao, Y., et al., 2020. Experimental study on the integrity of casing-cement sheath in shale gas wells under pressure and temperature cycle loading. J. Petrol. Sci. Eng. 195, 107548. https://doi.org/10.1016/j.petrol.2020.107548.

Deng, K.H., Zhou, N.T., Lin, Y.H., et al., 2023. Failure mechanism and influencing factors of cement sheath integrity under alternating pressure. Pet. Sci. 20 (4), 2413–2427. https://doi.org/10.1016/j.petsci.2023.03.004.

Du, W.F., Yang, H.Q., Huang, Z.Q., et al., 2021. The influence of cement sealing length on sealing capability under confining pressure. China Petrol. Mach. 49 (7), 53–58. https://doi.org/10.16082/j.cnki.issn.1001-4578.2021.07.008 (in Chinese).

Feng, Y.C., Li, X.R., Gray, K.E., 2017. Development of a 3D numerical model for quantifying fluid-driven interface debonding of an injector well. Int. J. Greenh. Gas Control 62, 76–90. https://doi.org/10.1016/j.ijggc.2017.04.008.

Hao, H., 2022. Cleaning functional spacer for improving sealing integrity and zonal isolation of cement sheath in shale gas wells: laboratory study and field application. SPE J. 27, 2226–2243. https://doi.org/10.2118/209220-PA.

Hu, X.H., Liu, S., Wen, C.Y., et al., 2025. Failure mechanism of zonal isolation for cement sheath induced by density reduction operations after liner casing cementing. ACS Omega 10 (18). https://doi.org/10.1021/acsomega.5c00006.

Kim, J., Moridis, G.J., Martinez, E.R., 2016. Investigation of possible wellbore cement failures during hydraulic fracturing operations. J. Pet. Sci. Eng. 139 (3), 254–263. https://doi.org/10.1016/j.petrol.2016.01.035.

Lecampion, B., Bunger, A., Kear, J., et al., 2013. Interface debonding driven by fluid injection in a cased and cemented wellbore: Modeling and experiments. Int. J. Greenh. Gas Control 18, 208–223. https://doi.org/10.1016/j.ijggc.2013.07.012.

Liu, Y., Li, Z.Q., Xia, J.G., et al., 2024. The novel compensated sector cement bond logging technology and application. In: Proceedings of the International Field Exploration and Development Conference 2023 (IFEDC 2023), pp. 514–522. https://doi.org/10.1007/978-981-97-0483-5_50.

Ramadan, M.A., Salehi, S., Kwatia, G., et al., 2019. Experimental investigation of well integrity: annular gas migration in cement column. J. Pet. Sci. Eng. 179, 126–135. https://doi.org/10.1016/j.petrol.2019.04.023.

Wang, H., Li, M., Wang, Q., et al., 2025. Recent advances and challenges of cement bond evaluation based on ultrasonic measurements in cased holes. Artif. Intell. Geosci. https://doi.org/10.1016/j.aiig.2025.100170.

Wang, H., Toksöz, M.N., Fehler, M.C., 2020. Wave propagation in a cased borehole and cement bond evaluation. In: Borehole Acoustic Logging – Theory and Methods. Petroleum Engineering. Springer, Cham. https://doi.org/10.1007/978-3-030-51423-5_4.

Wang, W., Dahi Taleghani, A., 2014. Three-dimensional analysis of cement sheath integrity around wellbores. J. Pet. Sci. Eng. 121, 38–51. https://doi.org/10.1016/j.petrol.2014.05.024.

Wang, Y.G., Feng, Y.C., 2024. Experimental and numerical simulation investigation of cement sheath integrity during multi-stage fracturing in offshore tight oil reservoir. J. Mar. Sci. Eng. 12 (5), 814. https://doi.org/10.3390/jmse12050814.

Wei, T., 2010. Logging Evaluation of Cementing Quality in Oil and Gas Wells. Petroleum Industry Press, Beijing (in Chinese).

Wu, X.N., Li, Z.Y., Hou, Z.M., et al., 2024. Analytical perspectives on cement sheath integrity: A comprehensive review of theoretical research. ACS Omega 9 (16), 17741–17759. https://doi.org/10.1021/acsomega.4c00475.

Wu, Z.Q., Yue, J.P., Li, Q., et al., 2018. Experimental study on the hydraulic seal integrity evaluation of casing-cement sheath bonding interface. China Offshore Oil Gas 30 (6), 129–134. https://doi.org/10.11935/j.issn.1673-1506.2018.06.016 (in Chinese).

Yan, X., Yao, Y., Guo, X.L., et al., 2024. Failure evaluation mechanism of cement sheath sealing integrity under casing eccentricity during multistage fracturing. Pet. Sci. 21 (5), 3428–3445. https://doi.org/10.1016/j.petsci.2024.04.013.

Zhou, S.M., Tao, Q., Yang, H.Q., et al., 2019. A sealing evaluation system for cement sheath in oil and gas wells. China Patent,. CN105352670B (in Chinese).